Boosting Gas-Phase TiO 2 Photocatalysis with Weak Electric Field Strengths of Volt/Centimeter

My Nghe Tran, Myriam Moreau, Ahmed Addad, Adrien Teurtrie, Thomas Roland, Vincent de Waele, Marc Dewitte, Louis Thomas, Gaëtan Lévêque, Chunyang Dong, et al.

Boosting gas phase TiO_2 photocatalysis with weak electric field strengths of V/cm

My Nghe Tran,[#,§] Myriam Moreau,[†] Ahmed Addad,[&] Adrien Teurtrie,[&] Thomas. Roland,[†] Vincent de Waele,[†] Marc Dewitte,[§] Louis Thomas,[§] Gaëtan Levêque,[§] Chunyang Dong,[#] Pardis Simon,[#] Karima Ben Tayeb,[†] David Mele,[§] Vitaly Ordomsky,[#] Bruno Grandidier[§*]*

[#] Univ. Lille, CNRS, Centrale Lille, ENSCL, Univ. Artois, UMR 8181 – UCCS – Unité de Catalyse et Chimie du Solide, F-59000 Lille, France.

[§] Univ. Lille, CNRS, Centrale Lille, Univ. Polytechnique Hauts-de-France, Junia-ISEN, UMR 8520 - IEMN, F-59000 Lille, France.

[†] Université de Lille, CNRS, UMR 8516 -500 LASIRE - Laboratoire de Spectroscopie pour les Interactions, 501 la Réactivité et l'Environnement, F-59000 Lille, France.

[&] CNRS, INRAE, Centrale Lille, UMR 8207 - UMET - Unité Matériaux et Transformations, Université de Lille, Lille F-59000, France.

KEYWORDS. TiO_2, photocatalysis, electric field, water splitting, toluene oxidation.

ABSTRACT. Among the semiconductor nanomaterials, titanium dioxide is at the forefront of heterogeneous photocatalysis, but its catalytic activity greatly suffers from the loss of photoexcited charge carriers through deleterious recombination processes. Here, we investigate the impact of an external electric field applied to conventional P25 TiO_2 nanopowder with or without Au nanoparticles to circumvent this issue. The study of two redox reactions in gas phase, water splitting and toluene degradation, reveals an enhancement of the photocatalytic activity with rather modest electric fields of a few V/cm only. Such an improvement arises from the electric field-induced quenching of the green emission in anatase, allowing the photoexcited charge carriers to be transferred to the adsorbed reactants instead of pointless radiative recombinations. Applying an external electric field across a trap-rich metal oxide material, such as TiO_2, which, when impregnated with Au nanoparticles, leads respectively to a twelve-fold and six-fold enhancements in the production of hydrogen and the oxidation of toluene for an electric field of 8 V/cm, without any electrolysis, is a simple and elegant strategy to meet higher photocatalytic efficiencies.

INTRODUCTION

Since the discovery of the photochemical activity of titanium dioxide with various organic solvents in 1956,[1] followed by the observation of an electrochemical photolysis of water more than a decade later,[2] the interest of using TiO_2 as a photocatalyst has grown steadily. Over the years, TiO_2 nanoparticles have supplanted the bulk form of TiO_2 in photocatalysis because of the higher density of photoexcited charge carriers and active sites at their surface. Being cheap, abundant, non-toxic, highly stable, while chemically active, this material has been widely exploited in heterogenous catalysis to produce H_2, reduce CO_2, fix N_2 and decompose pollutants.[3–8] Hence, it is recognized as a benchmark semiconductor photocatalyst,[9,10] in particular for gas phase reactions.[11–14] But it still faces with one major challenge. As a semiconductor material, it is prone to absorb light and generate electron-hole pairs in return. When both charge carriers are successful to reach the active sites of the TiO_2 surface, they can activate chemicals. Unfortunately, like many metal oxide materials, TiO_2 suffers from a high concentration of detrimental bulk point defects,[15] resulting in useless recombinations with rates faster than the time required to enable the reduction and oxidation of adsorbates at their surface.[10] Hence, the rapid recombination of the photogenerated electrons and holes strongly limits the quantum efficiency of TiO_2 as a photocatalyst.

To circumvent this issue, several strategies have been devised. Most of them rely on engineering specific structures in the photocatalyst to favor the separation of the photoexcited charge carriers.[16] For example, a photocatalyst containing two different phases of TiO_2 nanocrystals, such as anatase and rutile with two different band gaps, is good at trapping photogenerated electrons in the anatase nanocrystals, reducing the interaction between charge carriers of opposite sign and thus enhancing the chemical conversion in comparison with a pure

TiO_2 phase.[17] Similarly, the addition of noble metal nanoparticles to a photocatalyst consisting of semiconductor nanocrystals yields an increased photocatalytic activity as these co-catalysts scavenges the photoexcited electrons.[18] Doping metal oxide semiconductor nanocrystals with impurities allows the formation of defects, which trap one type of charge carriers, preventing their fast recombination with charge carriers of opposite sign.[19,20] Although all these strategies have led to improved photocatalytic performances, the chemical conversion is limited and cannot be further enhanced by increasing the amount of co-catalysts or the concentrations of impurities.

Electric polarization provides another route to increase the photoactivity of semiconductor materials. It can be achieved by increasing their optical absorption through the Franz-Keldysh effect, which requires electric fields of the order of 10^4 V/cm. Or, in quantum confined semiconductor materials, electric fields around 10^5 V/cm or higher are able to efficiently separate the charge carriers, the so-called Stark effect.[21–23] When the nanomaterials host an internal persistent polarization, such as ferroelectric metal oxide semiconductors, the charge carrier separation occurs for even smaller electric fields of 10^4 V/cm.[24] However, despite the absence of a spontaneous electric polarization in TiO_2, it turned out that applying electric fields of 10^2 V/cm to TiO_2 nanoparticles was successful to synthesize asymmetric Au-TiO_2 hybrids based on bipolar electrochemistry under illumination.[25] Moreover, similar electric field strengths gave enhanced photoactivity to TiO_2 thin films and microspheres for the degradation or removal of pollutants in solution.[26,27] These experiments point to a higher density of photoexcited charge carriers available for reactions thanks to the application of an external electric field (EEF). But these electric field strengths are much smaller than the ones required to meet an increased absorption through the Franz-Keldysh effect, an efficient charge carrier separation through the Stark effect or a self-cleaning process at the surface of TiO_2, as

theoretically predicted.[28] This discrepancy calls for a precise understanding of the actual EEF role in TiO_2 photocatalysis to cleverly design the next generation of photocatalysts.

In contrast to these works performed in solution, we investigate the impact of a modest in-plane electric field in gas phase reactions. Taking advantage of the use of mixed phases of TiO_2 and co-catalysts to enhance chemical conversions, as described above, we show the beneficial impact of an EEF for water splitting. The production of H_2 is found to linearly increase with the EEF, to reach a twelve-fold enhancement at an electric field of 8V/cm. This improvement results from the reduction of the radiative recombination process through trap states in TiO_2. It is evidenced by the quenching of the green emission in the anatase phase, hence promoting the activation of the chemicals by the photoexcited electrons. As the same mechanism accounts for the toluene oxidation in the gas phase, albeit to a reduced production increase, the concept of annihilating deleterious recombination processes with an EEF much smaller than the ones usually applied to separate photoexcited charge carriers in semiconductor nanoparticles is quite appealing as no electric current is required and the chip efficiently works in the gas phase.

RESULTS AND DISCUSSION

The successful impregnation of the Au nanoparticles (NPs) in the powder of TiO_2 nanocrystals was determined with high angle annular dark field scanning transmission electron microscopy (HAADF-STEM) (Figure 1a). Due to the significant atomic number of 79 for gold, which provides a Z-contrast much larger than the one of TiO_2 (Z=19),[29] the Au NPs show a bright contrast. Their identification was further confirmed by energy dispersive spectroscopy (EDS) analysis of Au element from the same area (Figure S1). Based on similar STEM images,

the Au NPs are randomly distributed. From the observation of 156 Au NPs, a mean size of 6.2 ± 3.9 nm is found (Figure 1b). High-magnification TEM images reveal the crystallinity of the different NPs (Figure 1c and Figure S2). The smaller interplanar distance seen in the Au NP departs from the interplanar distance of the TiO_2 nanocrystals, which consists, in the majority, of the anatase phase, and, to a lesser extent, of the rutile phases, as deduced from X-ray diffraction analyses (Figure S3).[30–33] Although the Au NPs are not hemispherical, the observation of truncated edges indicates the existence of contact areas between the Au NPs and the TiO_2 nanocrystals.[34] The small Au content of 1wt.% in the photocatalyst is further confirmed by UV-Vis diffuse reflectance measurements (Figure 1d). While the TiO_2 powder and Au/TiO_2 photocatalyst show a strong absorption below 400 nm, which is caused by the optical transitions occurring in TiO_2, an additional broad peak appears in the visible range for the Au/TiO_2 photocatalyst only. This peak becomes stronger with increasing amount of Au (Figure S4). It arises from the surface plasmon resonance of the Au metallic NPs.[35–38] The centre of the peak, around 540 nm, is consistent with the mean size of the Au NPs measured in TEM.[39] The metallic nature of the Au NPs is also confirmed by X-ray photoemission spectroscopy (XPS), as seen in Figure S5, with an Au $4f_{7/2}$ binding energy slightly smaller than that in pure Au foil (84.0 eV) consistent with the literature.[40]

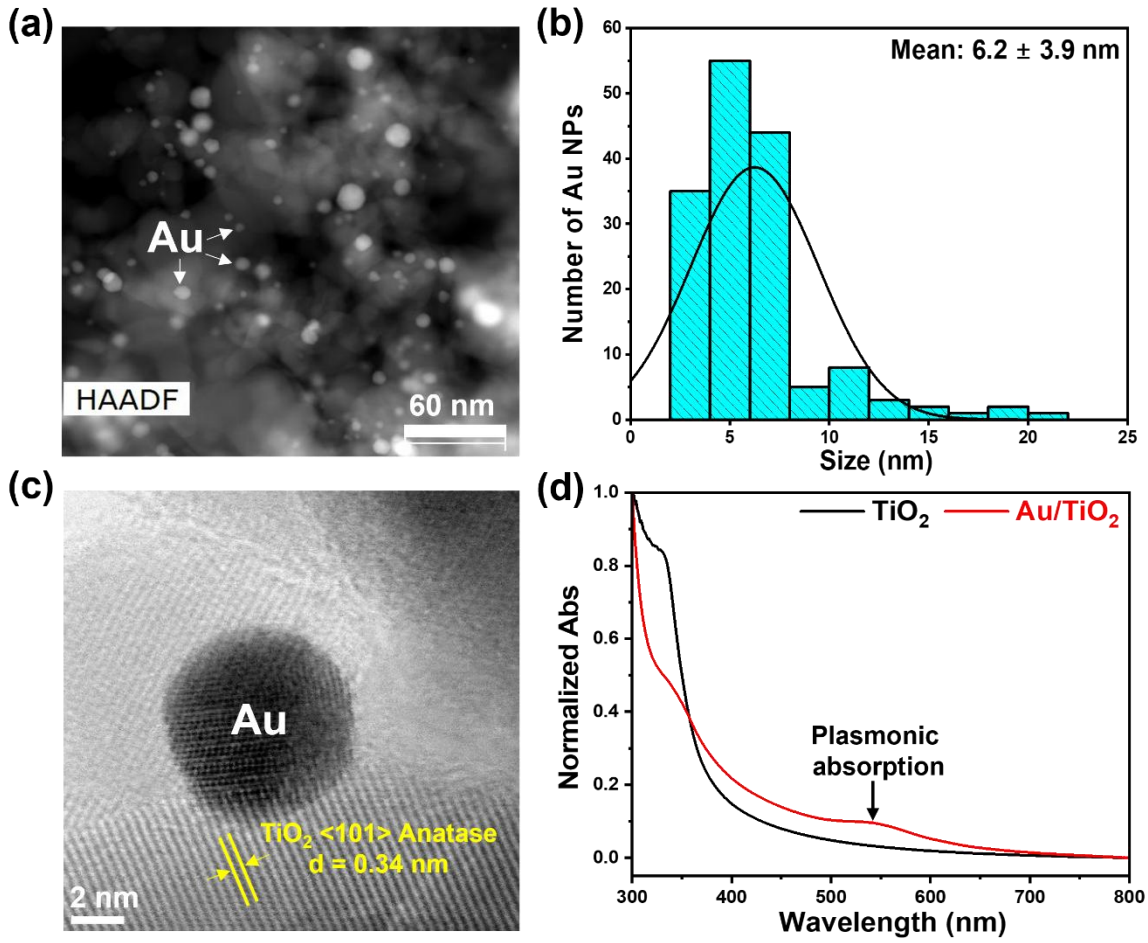

Figure 1. (a) HAADF-STEM micrograph of the Au/TiO_2 photocatalyst. (b) Related size distribution histogram. (c) HR-TEM image of an Au nanoparticle in contact with TiO_2 nanocrystals. (d) UV-Visible diffuse reflectance spectroscopy of the pure TiO_2 powder and the Au/TiO_2 composite.

The synthesized TiO_2 powder and the Au/TiO_2 powder were dissolved in ethanol and drop-cast on the whole surface of 2.5 × 2.5 cm^2 glass substrates, as shown in Figure 2a and as described in the preparation of the photocatalytic chips (Figure S6). Based on cross-sectional scanning electron microscopy, the average thickness of the layer was 17 µm. Without photocatalyst on the chip or light irradiation (back and red lines in Figure S7a), the chips did not

produce any gas in the presence of water at the bottom of the reactor, as schematized in Figure S8. Upon illumination of the chips with a Xe lamp, the photocatalytic H_2O splitting over pure TiO_2 sample generated only a minor amount of H_2 gas (nearly 120 µmol g^{-1}) after 15h of reaction (Figure S7b). Adding Au NPs in the TiO_2 powder allows to double the amount of H_2 gas, this production saturating about 240 µmol g^{-1} after 15h (black line in Figure 2b), a value consistent with the literature results of water splitting over Au/TiO_2.[41] Such an increase has been shown to result from the resonant surface plasmons of the Au NPs which provide hot carriers for reaction and enhances the local electric field at the interface between Au and TiO_2, favoring a stronger generation of electron-hole pairs.[42–44] Applying an EEF across the Au/TiO_2 chips shows a further increase of the production of H_2, which is roughly proportional to the applied bias (Figure S7c). The production does not change when the polarity is reversed (Figure S9). After 15 hours and for a bias of 20 V, it reaches 2991 µmol g^{-1}, which corresponds to a 12-fold increase in comparison with the production of H_2 in the absence of the EEF (green line in Figure 2b).

Similarly, all O_2 productions were much higher with a bias applied across the chips in comparison with experiments without any EEF (Figure S7d). In the absence of oxygen scavengers, water splitting should result in the generation of 0.5 O_2 molecules for each molecule of H_2. However, the amount of produced oxygen was lower than the produced hydrogen. We attribute this deviation to oxygen vacancies of the TiO_2 nanocrystals, which more likely adsorb oxygen generated during the reaction. Adsorbed O^- species were identified by the three *g* values of 2.006, 2.012 and 2.020 measured with electron paramagnetic resonance spectroscopy (Figure S10).[45–48] The adsorption of oxygen atoms was also detected with X-ray photoemission spectroscopy in ultrahigh vacuum, as a broader shoulder was measured at high binding energy on the O 1s core level in comparison with the composite chemical composition before water

splitting (Figure S11).[49] This efficient adsorption, which accounts for the lower production of oxygen, is also supported by regeneration treatments of the Au/TiO_2 chips by light and voltage in argon (Ar) resulting in the desorption of oxygen and recovery of the catalytic activity. While the regeneration process first consisted of irradiating the polarized Au/TiO_2 composite with 20 V for 8h, extending the duration of this process to 12h showed an enhancement of the H_2 production after the fourth run. Hence, the Au/TiO_2 photocatalytic chips demonstrated high activity after six consecutive cycles with a minor decline in H_2 production rate at the end (Figure 2c).

Importantly, applying only the EEF without illumination was unable to activate Au/TiO_2 for the production of H_2 and O_2 gas from H_2O (blue line in Figure S7a). Therefore, both light irradiation and an applied bias are essential for the photocatalytic H_2O splitting reaction. To get deeper insight into the impact of the EEF, the photocatalytic H_2O splitting tests over the Au/TiO_2 sample under the sequential applications of zero-bias and 20V were performed with 2 cycles for each type of condition (Figure 2d). The H_2 production rate increases from 240 to 2991 μmol g^{-1} after applying 20V, drops back to 224 μmol g^{-1} after switching off the voltage and recovers with the bias voltage. The detection of the same activity at zero bias during this sequence indicates the absence of remanent polarization in the sample. It also excludes a structural/chemical permanent change of the sample catalytic properties, which would be caused by the EEF.

For further evidence of the EEF effect and its suitability for various photocatalytic reactions, the toluene photodegradation reaction on the as-prepared Au/TiO_2 photocatalytic chip was also implemented (Figure 2e and Figure S7e). The photocatalytic oxidation of toluene by the Au/TiO_2 catalysts leads to the production of CO_2. The amount of CO_2 after 8 h of irradiation was 600 μmol g^{-1} at zero bias. It was significantly increased upon application of the EEF (5V, 10V and 20V). At the highest bias of 20V, the maximum production of CO_2 was 3542 μmol g^{-1},

yielding an almost 6-fold increase in the activity. It is consistent with the water splitting results and confirms that the EEF has a beneficial impact for two different photocatalytic reactions performed in the gas phase.

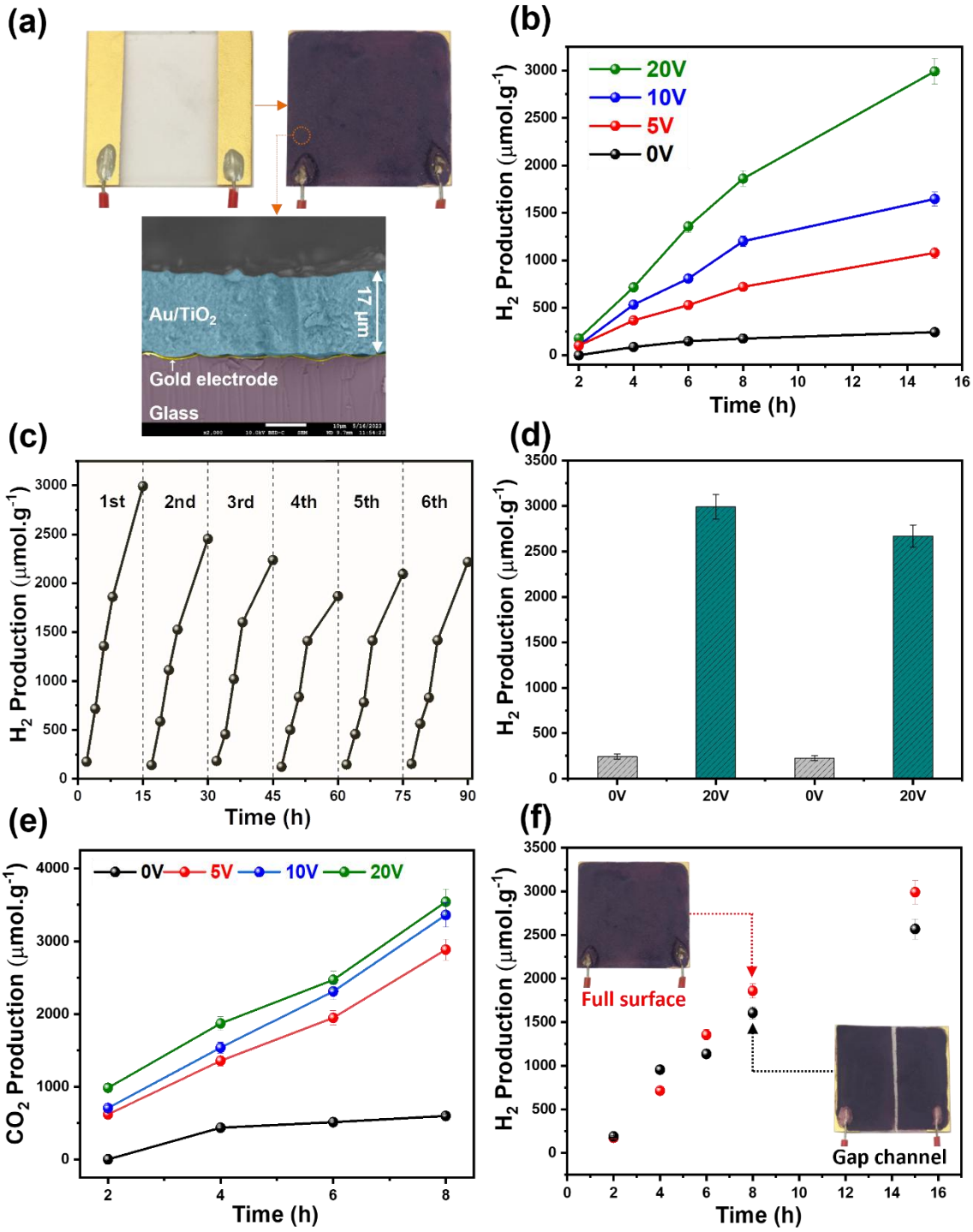

Figure 2. (a) Pictures of the chips before and after the deposition of the Au/TiO_2 photocatalyst and cross-sectional SEM image of the Au/TiO_2 supported over glass with a gold electrode layer in between. (b) H_2 production rates from H_2O splitting reactions as a function of irradiation time under different bias applied across the Au/TiO_2 chips. (c) Stability tests of the chips after regeneration of the Au/TiO_2 photocatalyst. (d) H_2 production rates from H_2O splitting under switching sequential different conditions from non-bias to applied bias at 20V. (e) CO_2 production rates for the photocatalytic oxidation of toluene as a function of irradiation time under different bias applied across an Au/TiO_2 chip. (f) Comparison of the H_2 production between a fully covered chip and a chip with a narrow gap in the middle of the sample, preventing any current from flowing across the chip. The error bars represent the standard deviations (SD) for three independent measurements.

In order to explain the positive impact of the EEF on the production yield, we measured the electric current flowing across the chips. Indeed, the higher activity obtained with a polarized chip can be caused by an electrocatalytic activation of the molecules. However, the current of a few nanoamperes is quite small and can barely affect the catalytic performance of the chips (Figure S12). More importantly, as seen in Figure 2f, a similar catalytic performance was found when a narrow gap exists in the middle of the chip, splitting the sample into two discontinuous parts (bottom inset in Figure 2f). As no current can flow across the polarized sample, this geometry rules out any contribution of the current to the enhanced activity of the polarized samples.

To get a deeper insight into the role of the applied bias for an enhanced photocatalytic performance, the optical properties of the Au/TiO_2 photocatalyst were investigated. At the nanoscale and without an EEF, spatially resolved STEM electron energy-loss spectroscopy (EELS) reveals a peak on the Au NP seen in Figure 3a. The peak is centred at an energy of 2.1

eV. It corresponds to the localized surface plasmon resonance of the Au NP[50] and is consistent with the broad plasmonic absorption measured with UV-Vis spectroscopy (Figure 1d). Based on the spectrum image acquired in the areas marked by the colour rectangles on the HAADF image, the peak shifts from 2.1 eV on the Au NP to 2.5 eV on the TiO_2 nanocrystals. This is better visible in the map of Figure 3b, where the position of the EELS peak in the TiO_2 nanocrystal varies between 2.3 and 2.6 eV, an energy range smaller than the band gap of rutile and anatase. These transitions have been identified as sub-bandgap transitions caused by oxygen vacancies.[51] They involve the radiative recombination of electrons in the conduction band and in shallow levels below the conduction band with trapped holes in deep levels, giving rise to the green photoluminescence (PL) in anatase.[10,52]

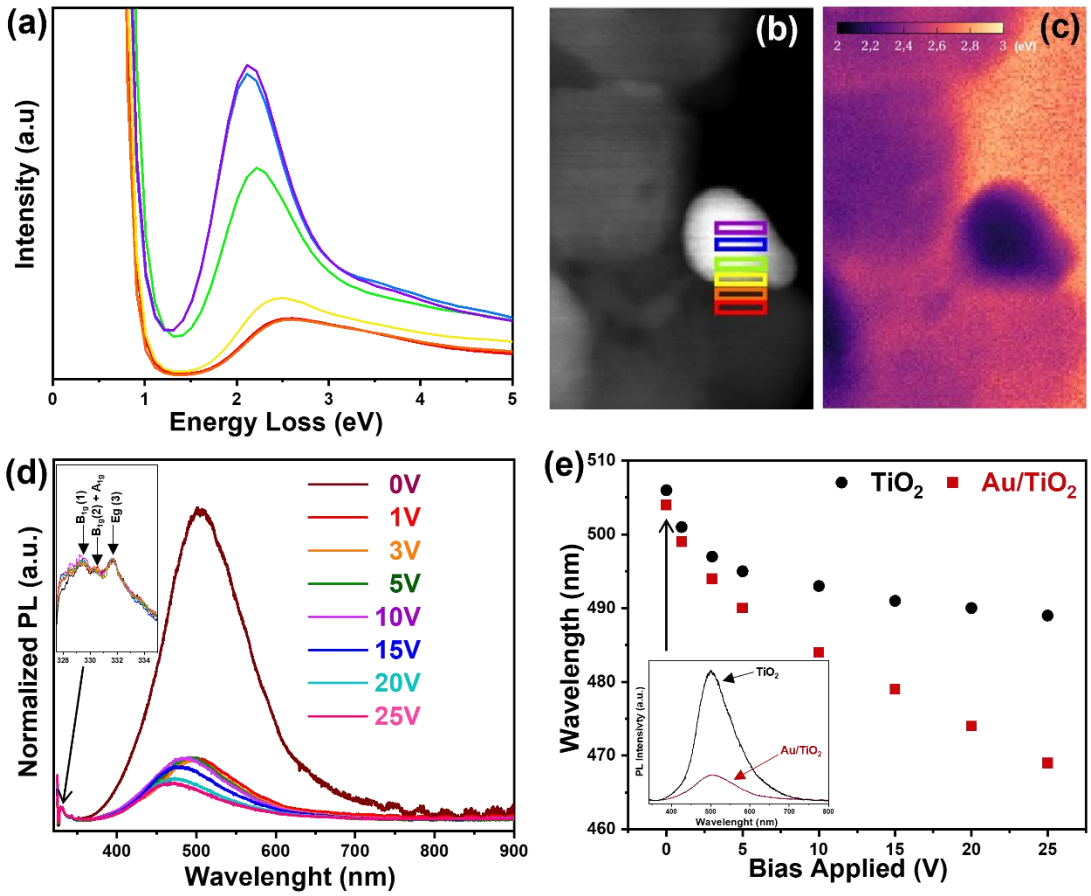

Figure 3. (a) Spatially resolved EESL spectra measured in the six areas delineated by the colour rectangles defined in (b) the HAADF-STEM image of a bright Au NP partially embedded in the dark-grey TiO_2 matrix. (c) Energy shift map of the EELS peak measured in the HAADF-STEM image shown in (b). (d) Photoluminescence (PL) spectra of the Au/TiO_2 photocatalyst for different applied biases. The spectra are normalized based on the measured Raman modes $B_{1g}(1)$, $B_{1g}(2)+A_{1g}$ and $E_g(3)$ which are highlighted in the inset. (e) Peak position of the PL spectra as a function of the applied bias for the TiO_2 P25 powder and the Au/TiO_2 photocatalyst. Inset: comparison of the PL emission between the P25 powder and the Au/TiO_2 photocatalyst at zero bias.

The existence of radiative transitions around 2.45 eV in the P25 and Au/TiO_2 chips is confirmed by PL experiments. Without any EEF, both chips show a broad peak centred at a

wavelength of 504 nm (inset of Figure 3d), in agreement with the PL peak found for anatase nanocrystals studied in air.[53,54] The peak is smaller for the Au/TiO_2 photocatalyst. This observation agrees with previous experimental results which have shown a reduction of the probability for photoexcited electrons to radiatively recombine with holes in TiO_2, the Au NPs scavenging the photoexcited electrons.[18,30,35] This transfer and its dynamics is highlighted with UV-Vis femtosecond transient absorption measurements of the Au/TiO_2 catalysts at the excitation of 350 nm. As shown in Figures 4a and b, the transient absorption spectra recorded for pump-probe delay up to 6 ns exhibits two clear distinct contributions: first, a negative contribution at the smallest wavelengths, which is strong below 400 nm and associated to the bleach of the band gap absorption of TiO_2; then, a second negative contribution in the visible spectral range, above 500 nm, which corresponds to the plasmonic response of the gold nanoparticles. As the kinetic of the non-geminate electron-hole recombination in TiO_2 varies with the concentration of photogenerated charge carriers,[55,56] and the hot-electrons dynamics in metal nanoparticles is governed by the amount of the energy absorbed by the metal,[57–59] two different pump intensities are used to record the transient spectra. The kinetic of the decay traces acquired at λ_{probe} = 420 nm and λ_{probe} = 560 nm for both pump intensities shows that the time evolution of the two contributions are clearly different (Figures 4(c-d)). Hence, in the Au/TiO_2 photocatalyst, the dynamics of the holes in the valence band of TiO_2 and the dynamics of the electrons in the conduction band of Au nanoparticles evolve independently. The analysis of the laser intensity on the kinetics reveals that the rate of recombination for the holes (λ_{probe} = 420 nm) decreases with the intensity, in good agreement with the second order kinetic expected for the non-geminate electron-hole recombination in TiO_2.[55,56] Conversely, for the plasmonic response of Au, the kinetics of the decays (λ_{probe} = 560 nm) is not affected by the pump intensity,

the decay being much slower (τ = 7 ps) than the typical electron-phonon coupling rate in gold or silver nanoparticles (τ < 1 ps).[57–59] Therefore, the measured perturbation of the plasmonic response is not caused by the direct excitation of the electrons in the metal. It arises from the electron transfer between the TiO_2 nanocrystals and the Au NPs, in agreement with the measured decrease of the PL for the Au/TiO_2 photocatalyst with respect to the P25 sample.

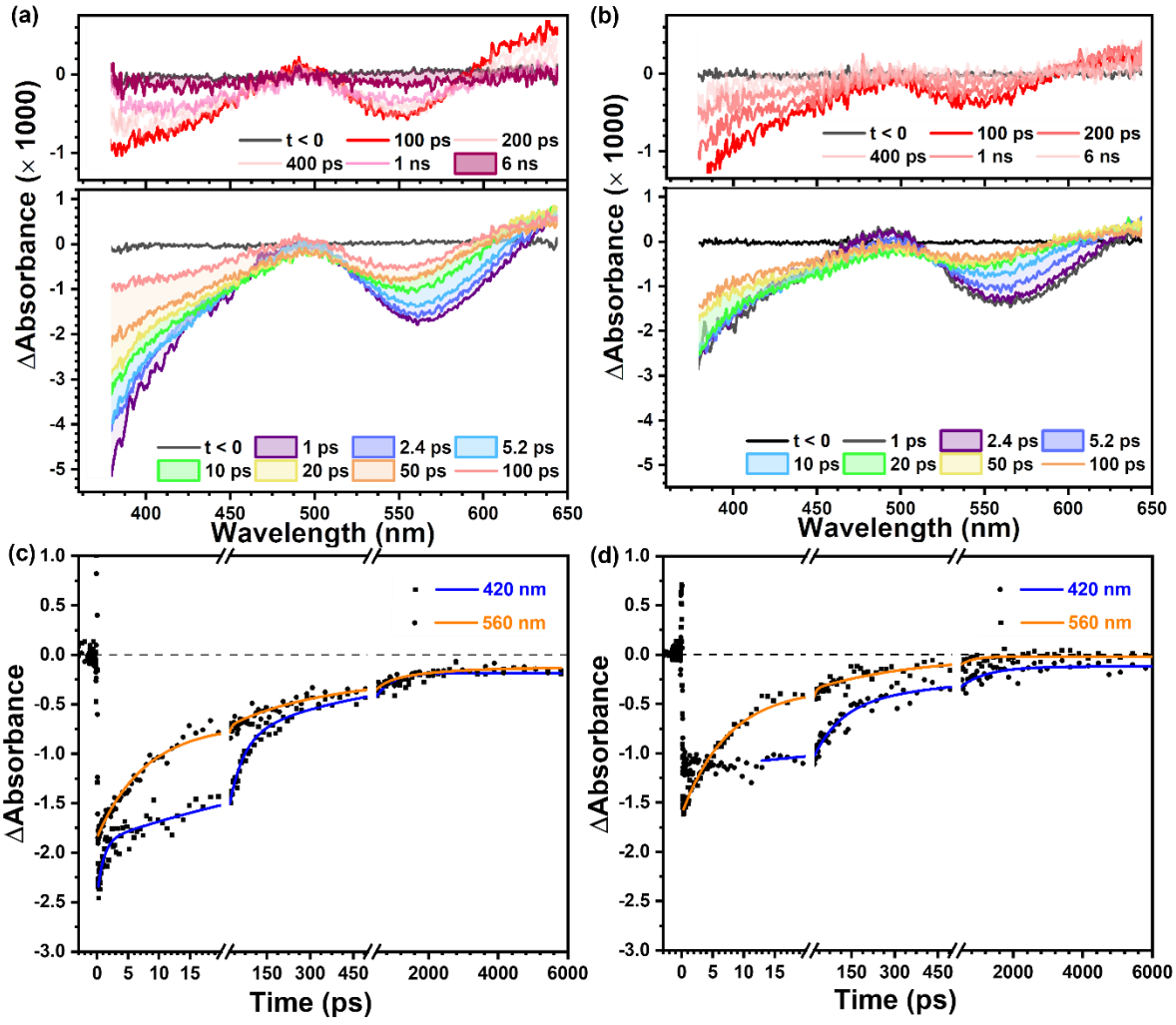

Figure 4. (a-b) Transient spectra and (c-d) kinetic traces recorded upon photoexcitation of the Au/TiO_2 photocatalyst with λ_{pump} = 350 nm of relative intensity I_0 (data a, c) and $I_0/2$ (data b, d), respectively. In a), b), the legend corresponds to different pump-probe delays. In (c) and (d), the kinetic traces are

reconstructed for the transient spectra for the probe wavelengths λ_{probe} = 420 nm and λ_{probe} = 560 nm. The coloured lines correspond to the best fits by three exponential decay model functions.

The PL of Au/TiO_2 sample was further studied as a function of the bias across the chip at ambient conditions. By normalizing the spectra based on the small Raman peaks used as a reference (inset of Figure 3c and Figure S13), we have observed that a small bias of 1V decreased the PL signal (Figure 3c). Larger bias led to a stronger suppression of the PL. The quenching predominantly affects the lowest transitions, resulting in a small decrease of the peak linewidth by 13 nm and a significant blue-shift by 39 nm (Figure 3d), when the applied bias reaches 25 V for the Au/TiO_2 chip.

To understand the influence of the EEF on the PL, the variation of the potential across the samples was measured with Kelvin probe force microscopy (KPFM). While the 1 x 1 μm² AFM images acquired in five different areas on the Au/TiO_2 chip (marked in Figure 5b) show a similar morphology, the 1 μm-long KPFM line scans reveal a clear change of the contact potential as the AFM tip moves from one area to the next one with increasing bias applied to the left electrode (Figure 5a). By plotting the contact potential difference (CPD) as a function of the distance for biases in the range 0 to 10 V (Figure 5c), all the traces can be approximated by a linear slope away from the electrodes, indicating that the EEF corresponds to the applied voltage divided by the sample width. This observation dismisses the existence of areas with intense EEF in the sample. Therefore, a continuous and smooth drop of the potential between the electrodes yield a maximum constant electric field of 8 V/cm, much too weak to produce a Stark effect able to separate the photoexcited electrons and holes in the TiO_2 nanocrystals.[21–23]

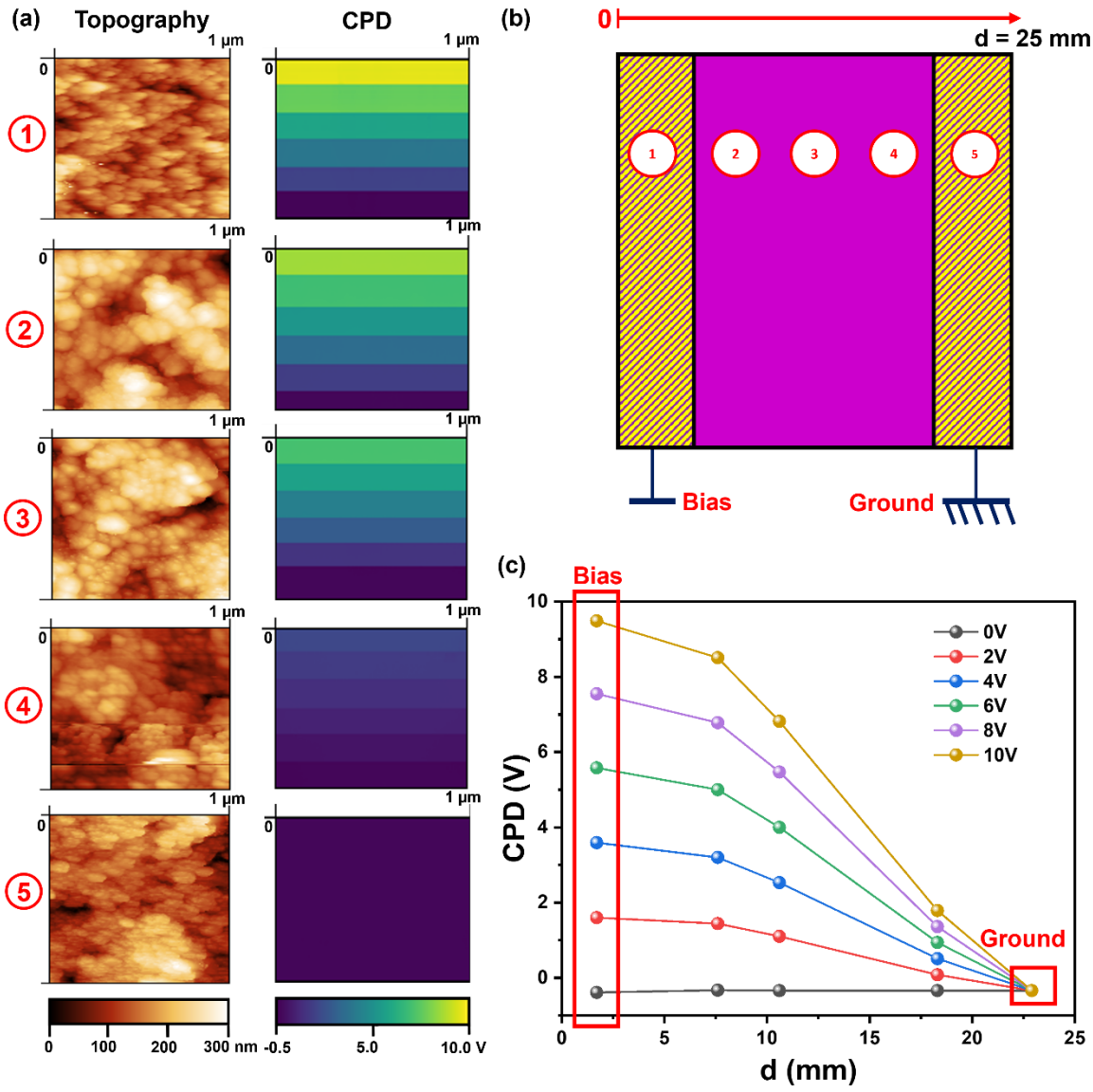

Figure 5. (a) Topography images of the sample surface acquired at five equidistant locations across the sample width and contact potential difference (CPD) lines measured in the middle of the AFM image with increasing polarization by steps of 2V. (b) Schematic of the sample highlighting the five areas, where the KPFM measurements were performed. (c) Variation of CPD as a function of the distance d from the left electrode for different biases V applied on this electrode.

Albeit weak, it can ionize the shallowest levels below the conduction band of anatase,[52,60] preventing the photoexcited electrons to recombine with holes trapped in deep levels about 2.4 eV below the conduction band (Figure 6 for water splitting and Figure S14 for toluene oxidation reactions). Therefore, these electrons are available at the anatase nanocrystal surfaces and interfaces to be transferred to the rutile or Au NPs and/or activate the reactants. As the field ionization of the shallow states leads to a partial filling of the conduction band states, a few radiative transitions can still occur, but they involve electrons with slightly higher energies than the bottom of the conduction band. The so-called Burnstein-Moss effect in semiconductor materials would explain the observed blue-shift of the weak and remaining PL for both the P25 and Au/TiO_2 chips.[61,62] As the radiative recombination pathway is suppressed, the excess of available electrons reacts not only with hydrogen, but also oxygen molecules, producing superoxide species. As shown in Figure 6, the chemisorbed superoxides, which are negatively charged, causes an upward band bending at the surface of the anatase nanocrystals.[54,60] The resulting depletion layer contributes further to the quenching of the green PL.

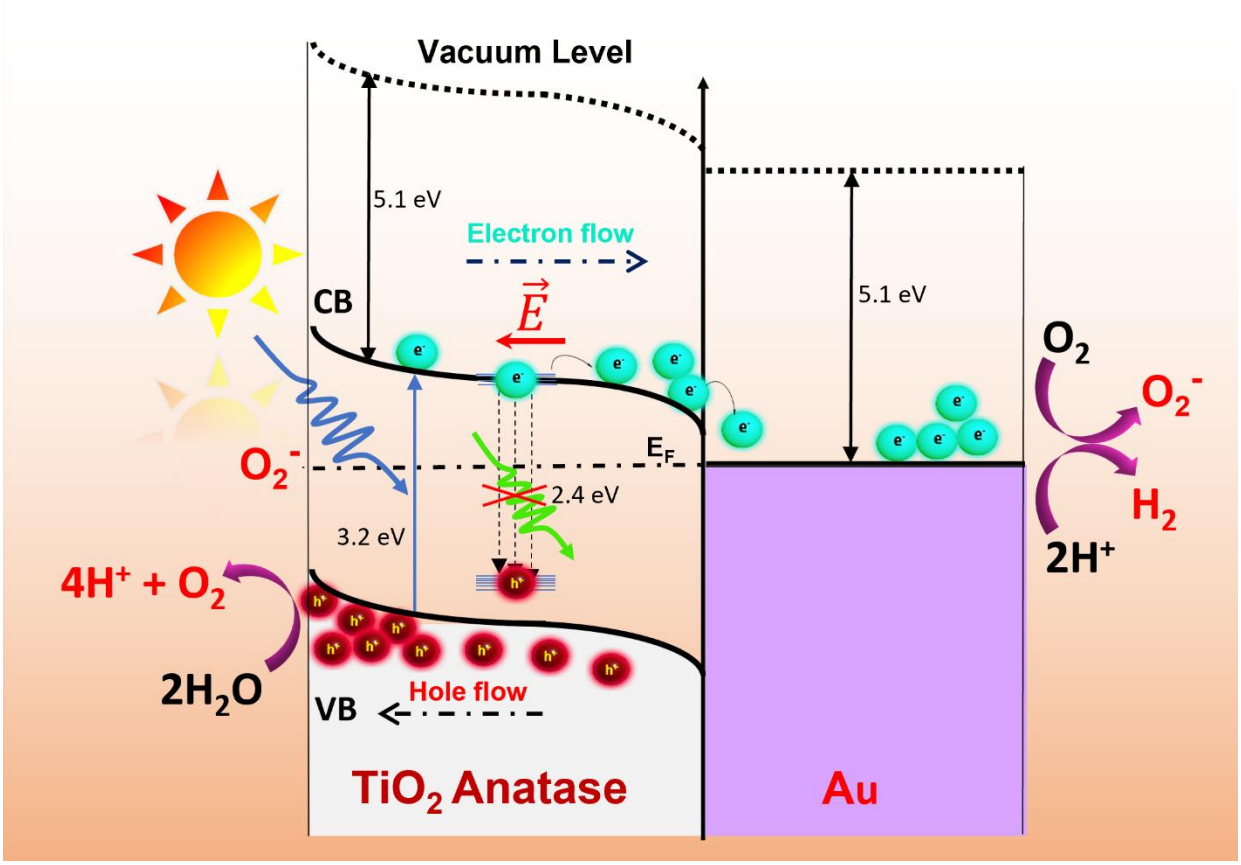

Figure 6. Band diagram of the heterointerface between gold and TiO_2 with the anatase crystal structure for water splitting. The Fermi level, conduction and valence bands are labelled E_F, CB, and VB respectively. The TiO_2 nanocrystals are usually oxygen deficient giving them a n-type character.[54] $\vec{E}$ corresponds to the applied external electric field, which excites the electrons in the shallowest levels to the conduction band. The work function of Au is taken as the bulk one, although it might be smaller for Au NPs.[63] The electron affinity of anatase is taken from Ref. 64. The values of the band gap and electron affinity for anatase TiO_2, the energy of the hole trap-states distribution from the bottom of the conduction band and the work function of gold are indicated. The reactions are sketched on both sides of the band diagram. They involve the oxidation of water by photogenerated holes with the production of dioxygen and protons, and the reduction of the protons by photogenerated electrons yielding H_2 as the main product. An alternative exists with the creation of a superoxide anion which adsorbs on the surface of the TiO_2 nanocrystals.

To explain the stronger blue-shift measured in the Au/TiO_2 chips in comparison with the P25 chips, we simulated the absorption cross-section of a gold NP embedded in an insulating environment with a mean dielectric constant of 1.7 using Mie theory. We assume that the quenching of the PL due to the EEF causes a more effective charge transfer of the electrons to the Au NPs, as seen in Figure 6. This effect leads to an increase of the electron density at the surface of the Au NPs.[65] By simulating the extinction cross-section with higher and higher electron densities N with respect to the electron density N_0 at zero bias, Figure 7 shows that the plasmonic resonance is clearly blue-shifted (see also Figure S15 for different dielectric constants), in agreement with a plasma frequency of the Au NPs varying as the square root of the carrier density.[66,67] Therefore, our result suggests that the observed PL peak in the Au/TiO_2 chips have two contributions, the green emission related to TiO_2 and an emission from the Au NPs. Although very weak, the latter one would explain the stronger blue-shift in the Au/TiO_2 chips in comparison with the P25 chip, when the green emission becomes significantly reduced.

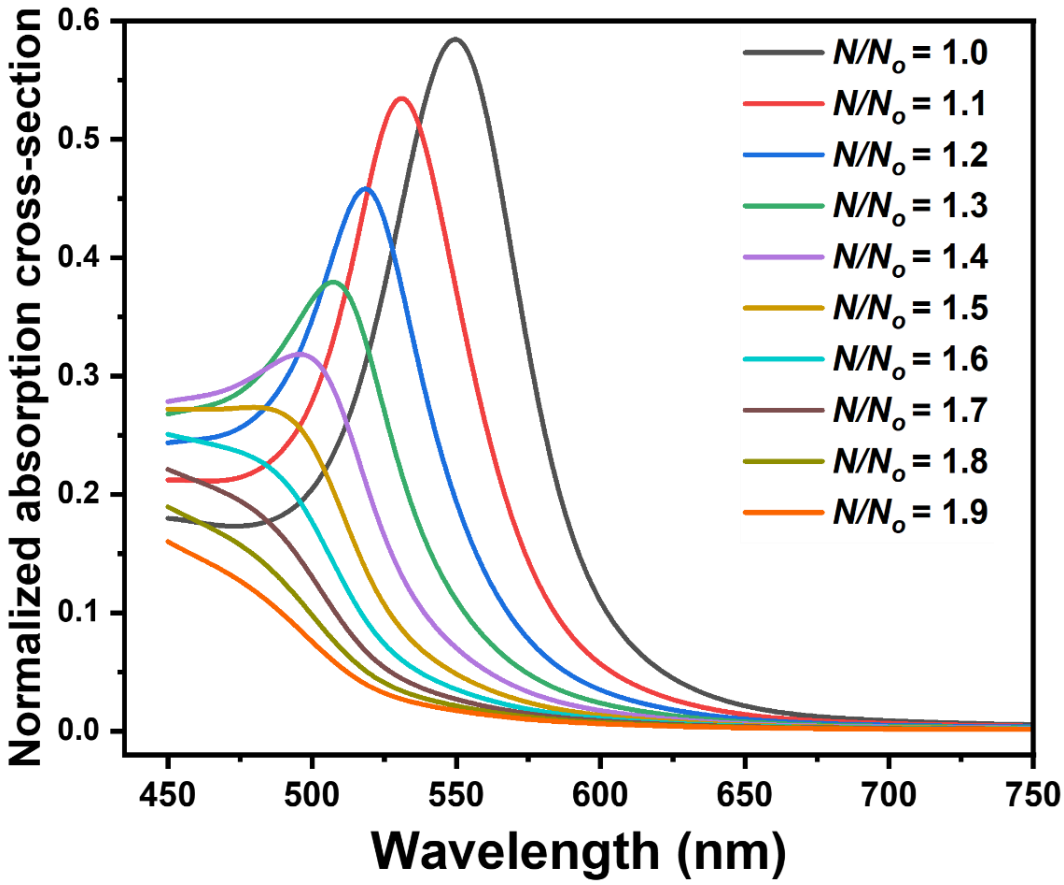

Figure 7. Simulation of the absorption cross-section for a gold nanoparticle with a diameter of 6.2 nm in an insulating environment with a mean dielectric constant of 1.7, for increasing electron densities ratio N/N_0 in gold. N_0 corresponds to the electron density at zero bias.

CONCLUSION

In summary, we have found an increase in the photocatalytic activity assisted by an external electric field for water splitting on the Au/TiO_2 heterostructure. Based on the analysis of the PL emission as a function of the sample polarization, the improved performance of the

photocatalyst arises from the increasing quenching of the radiative recombination between the photoexcited electrons and holes in the TiO_2 nanocrystals. We attribute this quenching to the synergetic action between the electric-field assisted electron emission in TiO_2 and the conversion of oxygen to chemisorbed superoxides at the TiO_2 surface, which makes the slow charge transfer of electrons to reactants competitive with the recombination process. As many metal oxide semiconductors are prized in photocatalysis and enclose shallow trap states, the application of an EEF provides an efficient and low-cost route to substantially improve their photocatalytic activity by suppressing deleterious recombination processes.

METHODS

Materials and reagents

Titanium (IV) oxide powder (TiO_2, P25, 99.5%), toluene liquid (C_7H_8, ACS reagent, 99.5%), gold (Ⅲ) chloride tetrahydrate ($HAuCl_4 \cdot 4H_2O$), sodium borohydride powder ($NaBH_4$, 98%) and ethyl alcohol (C_2H_5OH) were purchased from Sigma-Aldrich. Deionized (DI) water was used as solvent for material cleaning steps. Nitrogen gas, argon gas and synthetic air were provided by Air Liquide company. All chemicals were used without further purification.

Preparation of photocatalytic chips

The fabrication of photocatalytic chips consists in two steps including photocatalyst synthesis and deposition of the photocatalyst on the substrates. First, the Au/TiO_2 photocatalyst was typically prepared via the incipient wetness impregnation method (Figure S6a). For this, TiO_2 powder (0.5 gram) was dissolved with DI water (50 mL) in a glass container before being vigorously stirred for 20 min. Afterwards, 40 µL of gold precursor solution ($HAuCl_4 \cdot 4H_2O$, 0.625 M) was slowly added to the obtained slurry and kept on the stirrer for next 10 min.

Subsequently, the reductive $NaBH_4$ solution (2 mL, 0.05 M) was slightly poured into this suspension, which was immediately turned into dark purple color. After being stirred for further 10 min, the slurry was centrifugated to remove solvent and washed several times with DI water and ethanol. Eventually, the obtained powders were dried at 60 ^oC overnight, then calcinated at 300 ^oC for 4h before being stored in a vial for next experiments. The weight percent (wt.%) of Au NPs loading in Au/TiO_2 photocatalyst was estimated at 1%. To compare the optical properties, another Au/TiO_2 sample with higher Au NPs content (3%) was synthesized in the similar way.

Along with the synthesis of catalysts, chips were prepared from pieces of glass (2.5 cm×2.5 cm), which were first immersed in a HF solution for 5 min to enhance their surface roughness. Then, they were washed several times with ethanol and DI water to get rid of HF acid residue. Subsequently, two gold electrodes with rectangular shapes (0.5 cm × 2.5 cm) were deposited for 4 min at a rate of 0.5 nm/s along the two opposite edges of the glass substrate by using an evaporation system (Plassys MEB E-beam 550S). Shortly afterwards, two electrical wires were subsequently attached on gold electrodes by silver paste for receiving external bias (Figure S6b). The distance between the electrical wires was fixed at 2 cm. Finally, the chips were dried at 80 ^oC for 3h. The second step in the chip preparation consisted in dissolving 10 mg of the synthesized Au/TiO_2 powder in ethanol and drop-casting it on the whole surface of the chips.

Characterization and measurement

The crystal structure and chemical composition of the Au/TiO_2 photocatalyst and the TiO_2 were inspected by X-ray diffraction (XRD), equipped with a Cu-Kα radiation source working at 40 kV and 30 mA (Empyrean system from Panalytical). The crystalline phases were

determined based on the diffraction patterns with those of the standard powder X-ray diffraction files (JCPDS).

Morphologies and high-resolution atomic arrangements of the synthesized photocatalysts were examined by using a scanning transmission electron microscopy (S/TEM, TITAN Themis 300) mounted with an HAADF detector (electron energy of 300 keV). Element mapping of samples was performed with energy-dispersive X-ray spectroscopy (EDS). The optical absorption of photocatalysts was studied with the Ultraviolet–Visible diffuse reflectance spectroscopy (UV-Vis DRS) using a spectrometer (PerkinElmer Lambda 650S).

For X-ray photoelectron spectroscopy (XPS), we used a Kratos Axis Ultra DLD photoelectron spectrometer using monochromatic Al Ka (1486.7 eV) X-ray irradiation. High-resolution spectra were collected after loading the samples in ultrahigh vacuum with an analysis area of 300μm - 700 μm and a 20-eV pass energy. The binding energies were measured after surface charging corrections with the spectrometer and work function of the instrument calibrated based on the binding energy of the Au $4f_{7/2}$ peak at 84.0 eV measured on a clean Au foil.

The analysis of paramagnetic species was performed by continuous-wave electron paramagnetic resonance (EPR). These experiments were performed on a Bruker ELEXSYS E500 spectrometer operating in the X-band (9.5 GHz). The following conditions were used for the in-situ measurements: a microwave power of 2 mW and modulation amplitude of 1 G with a conversion time of 82 ms and 30 scans. The EPR spectra were recorded at 94K to avoid electron-hole recombination.

The photoluminescence spectra were measured with a 325 nm excitation (HR Labram, Horiba Scientific), either without or with an external electric field. During the measurement of a

spectrum, the bias was kept constant, and the measurements were repeated by varying the voltages between 0 and 25 V. As the samples are not conductive and get charged upon illumination, the elapse time between two measurements was set to 20 minutes to restore the intrinsic properties of the samples. To be able to compare the spectra despite residual charging effects, they were normalized with respect to the Raman peaks measured at 329.3 nm, 330.5 nm and 331.8 nm (inset of Figure 3c). The corresponding wave numbers of 401 cm^{-1}, 512 cm^{-1} and 631 cm^{-1} match well with the position of the peaks measured in the Raman spectra of the P25 powder (Figure S13) and arising from anatase TiO_2. [30,68]

The optical properties of individual Au NPs in the TiO_2 matrix were also analysed with STEM operated at 200 keV and combined with electron energy loss spectroscopy (EELS). Using the scanning beam mode, the electron beam was focused to a point which was scanned to form an image, the so-called spectrum-image mode. The EELS spectra were recorded from a small excited volume by collecting low-angle scattered electrons. The achieved energy resolution, measured as the full width at half maximum of the zero-loss peak (ZLP), was approximately 0.4 eV. The contribution of the ZLP tail was significantly reduced by means of the Richardson−Lucy deconvolution using the ZLP spectrum captured in vacuum.

The femtosecond laser pulses were generated by using a Ti:Sa chirped-pulse amplifier (CPA) laser (model Astrella from Coherent) delivering 35 fs pulses at 800 nm, 1kHz and with an energy of 5.5 mJ per pulse. After passing through a telescope, the main part of the beam (2.7 mJ) was reflected by a 50/50 beam splitter and it was steered into a first OPA (Model OPERA from Coherent) while 1.8 mJ (70%) of the transmitted beam was seed into a second OPA (Model OPERA from Coherent). A small part of the residual beam at 800 nm was used to generate the supercontinuum probe beam in the transient absorption spectrometer. The OPAs were used to

generate the pump pulses whose wavelength is tuneable in the 250 nm-1600 nm spectral range. For these experiments, the pump excitation was set to 350 nm or 700 nm, with an energy per pulse of less than 500 nJ on the sample. The intensity of the pump was adjusted by using a 0.3 or 0.6 optical density. The transient absorption signal was measured in transmission with a transient absorption spectrometer (model HELIOS from UltrafastSystems) equipped with an auto-aligned 7 ns long optical delay line and three supercontinuum (SC) generation stages covering the full UV to NIR spectral range. After the generation, the SC beam was split into a Signal (SIG) and Reference (REF) beam, both detected by a UV-vis or NIR multichannel detector. Only the SIG beam was passing through the sample, which consisted of the TiO_2/Au (1%) photocatalyst deposited on a thin BK7 glass window. The pump beam was steered into the sample by using reflective optics and it was focused by a off-axis parabolic mirror. The relative polarization between the pump and probe beam was adjusted at the magic angle using a Berek compensator.

KPFM was performed with a Bruker Dimension 3100 AFM operating under ambient conditions in amplitude-modulation (AM)-lift KPFM mode with a Pt/Ir coated silicon probe (Nanosensors PPP-EFM). In a first pass, the microscope operates in tapping mode, then the tip is lifted by 50 nm and an AC + DC bias is applied to the tip. The amplitude of the AC component was set to 6V and its frequency to the resonant frequency of the probe (82.6 kHz) while the KPFM feedback loop adjusts the DC bias to nullify the oscillation of the probe. As a result, its value equals the CPD between the tip and the sample. We first imaged the area of interest at 0 V sample bias revealing a homogeneous CPD between -0.26 and -0.45 V. Then, the scan frame was restarted from the bottom, disabling the slow scan axis while increasing the sample bias from 0 to +10V by step of 2V.

Simulation

The normalize cross-sections of a spherical gold nanoparticle embedded inside a homogeneous transparent medium has been simulated using Mie theory.[69] The dielectric constant of the bulk gold has been modified by applying a correction to the free electrons contribution with the following relation derived from reference[70]:

$$\epsilon_r(\omega) = \epsilon_{r0}(\omega) - \frac{\omega_p^2}{\omega(\omega - i\Gamma)}\left(1 - \frac{N}{N_0}\right)$$

where ω is the angular frequency, $\hbar\omega_p$=9.0 eV, $\hbar\Gamma$=70 meV, N and N_0 are the free electrons densities of the biased and unbiased bulk gold respectively, and $\varepsilon_{r0}(\omega)$ the dielectric constant of unbiased bulk gold from reference.[71] The refractive index of the environment has been fixed to $n=1.7$ in order to reproduce the correct position of the unbiased plasmon resonance at λ=550 nm. Finally, cross-sections have been normalized to the section of the nanoparticle, $\sigma_0=\pi R^2$ where R is the nanoparticle's radius.

Photocatalytic tests

The external electric field-assisted photocatalytic activities of H_2O splitting toward Au/TiO_2 catalyst were conducted in a stainless-steel batch reactor (250 mL) with a transparent window on the top (Figure S8). A solar simulator (CHF-XM 500W) with full irradiation was used as a light source. The electrical wires were plugged to a power supply (DC power supply AL 924A), which provides the external electric field for photocatalytic reactions.

To perform the H_2O splitting reaction, the batch reactor containing the photocatalyst chip in the middle of the reactor and 10 ml of DI water on the bottom was evacuated by a vacuum pump for 30 min, then charged by argon gas (1 MPa) as a medium. The toluene decomposition was similarly conducted by evacuating the batch reactor containing the photocatalyst chip before providing a mixture of toluene vapor and synthetic air (0.5 MPa). The toluene vapor was created

in a metallic container by purging toluene liquid with purity N_2 gas at room temperature. The concentration of toluene vapor was estimated at 3000 ppm. Afterwards, the reactor was kept in dark condition for 30 min to obtain an adsorption-desorption equilibrium between the photocatalysts and reactant molecules prior to light irradiation.

The reactor was maintained at 25±2 °C for both types of reactions by using a cooling system. After the reaction, the gaseous products were directly injected and analyzed by a gas chromatography (GC, Aglient 8860) combined with a flame ionization detector (FID) and a thermal conductivity detector (TCD). To regenerate the active surface of the catalyst, the used Au/TiO_2 chip was simultaneously polarized at 20V and treated under light irradiation for 8h in the presence of only argon gas before running new cycles.

ASSOCIATED CONTENT

The Supporting Information is available free of charge on the ACS Publications website at DOI:

Details of the synthesis of the Au/TiO_2 photocatalyst powder, the sample fabrication and the equipment for the photocatalytic reactions. Additional TEM data. XRD patterns. Control experiments for the H_2 production. O_2 production rates from H_2O splitting reactions as a function of irradiation time under different bias applied across the Au/TiO_2 chips. I(V) characteristics. Transient absorption spectra. Raman spectrum of the TiO_2 P25 powder. Band diagram for the toluene oxidation. Simulation of the extinction cross-sections for a gold nanoparticle.

AUTHOR INFORMATION

Corresponding Author

*email: bruno.grandidier@univ-lille.fr, vitaly.ordomsky@univ-lille.fr

Author Contributions

The manuscript was written through contributions of all authors. All authors have given approval to the final version of the manuscript.

Funding Sources

This project has received funding from the European Union's Horizon 2020 research and innovation program under the Marie Skłodowska- Curie grant agreement N°847568.

ACKNOWLEDGMENT

The authors acknowledge the support of the Chevreul institute and IEMN PCMP-PCP platform within the RENATECH network.

REFERENCES

(1) Kato, S.; Mashio, F. Abtr. Book Annu. Meet. Chemical Society of Japan 1956.

(2) Fujishima, A.; Honda, K. Electrochemical Photolysis of Water at a Semiconductor Electrode. *Nature* **1972**, *238* (5358), 37–38.

(3) Fujishima, A.; Zhang, X.; Tryk, D. A. TiO_2 Photocatalysis and Related Surface Phenomena. *Surf. Sci. Rep.* **2008**, *63* (12), 515–582.

(4) Ola, O.; Maroto-Valer, M. M. Review of Material Design and Reactor Engineering on TiO2 Photocatalysis for CO_2 Reduction. *J. Photochem. Photobiol. C Photochem. Rev.* **2015**, *24*, 16–42.

(5) Hirakawa, H.; Hashimoto, M.; Shiraishi, Y.; Hirai, T. Photocatalytic Conversion of Nitrogen to Ammonia with Water on Surface Oxygen Vacancies of Titanium Dioxide. *J. Am. Chem. Soc.* **2017**, *139* (31), 10929–10936.

(6) Pichat, P.; Disdier, J.; Hoang-Van, C.; Mas, D.; Goutailler, G.; Gaysse, C. Purification/Deodorization of Indoor Air and Gaseous Effluents by TiO2 Photocatalysis. *Catal. today* **2000**, *63* (2–4), 363–369.

(7) Dong, C.; Marinova, M.; Tayeb, K. Ben; Safonova, O. V; Zhou, Y.; Hu, D.; Chernyak, S.; Corda, M.; Zaffran, J.; Khodakov, A. Y. Direct Photocatalytic Synthesis of Acetic Acid from Methane and CO at Ambient Temperature Using Water as Oxidant. *J. Am. Chem. Soc.* **2023**, *145* (2), 1185–1193.

(8) Hu, D.; Addad, A.; Tayeb, K. Ben; Ordomsky, V. V; Khodakov, A. Y. Thermocatalysis Enables Photocatalytic Oxidation of Methane to Formic Acid at Room Temperature beyond the Selectivity Limits. *Cell Reports Phys. Sci.* **2023**, *4* (2).

(9) Guo, Q.; Zhou, C.; Ma, Z.; Yang, X. Fundamentals of TiO_2 Photocatalysis: Concepts,

Mechanisms, and Challenges. *Adv. Mater.* **2019**, *31* (50), 1901997.

(10) Lettieri, S.; Pavone, M.; Fioravanti, A.; Santamaria Amato, L.; Maddalena, P. Charge Carrier Processes and Optical Properties in TiO_2 and TiO_2-Based Heterojunction Photocatalysts: A Review. *Materials (Basel).* **2021**, *14* (7), 1645.

(11) Verbruggen, S. W. TiO2 Photocatalysis for the Degradation of Pollutants in Gas Phase: From Morphological Design to Plasmonic Enhancement. *J. Photochem. Photobiol. C Photochem. Rev.* **2015**, *24*, 64–82.

(12) Shayegan, Z.; Lee, C.-S.; Haghighat, F. TiO2 Photocatalyst for Removal of Volatile Organic Compounds in Gas Phase–A Review. *Chem. Eng. J.* **2018**, *334*, 2408–2439.

(13) de Brito Lira, J. O.; Riella, H. G.; Padoin, N.; Soares, C. An Overview of Photoreactors and Computational Modeling for the Intensification of Photocatalytic Processes in the Gas-Phase: State-of-Art. *J. Environ. Chem. Eng.* **2021**, *9* (2), 105068.

(14) Qi, M.-Y.; Conte, M.; Anpo, M.; Tang, Z.-R.; Xu, Y.-J. Cooperative Coupling of Oxidative Organic Synthesis and Hydrogen Production over Semiconductor-Based Photocatalysts. *Chem. Rev.* **2021**, *121* (21), 13051–13085.

(15) Pastor, E.; Sachs, M.; Selim, S.; Durrant, J. R.; Bakulin, A. A.; Walsh, A. Electronic Defects in Metal Oxide Photocatalysts. *Nat. Rev. Mater.* **2022**, *7* (7), 503–521.

(16) Peiris, S.; de Silva, H. B.; Ranasinghe, K. N.; Bandara, S. V; Perera, I. R. Recent Development and Future Prospects of TiO2 Photocatalysis. *J. Chinese Chem. Soc.* **2021**, *68* (5), 738–769.

(17) Ohno, T.; Tokieda, K.; Higashida, S.; Matsumura, M. Synergism between Rutile and Anatase TiO_2 Particles in Photocatalytic Oxidation of Naphthalene. *Appl. Catal. A Gen.* **2003**, *244* (2), 383–391.

(18) Gomes Silva, C.; Juárez, R.; Marino, T.; Molinari, R.; García, H. Influence of Excitation Wavelength (UV or Visible Light) on the Photocatalytic Activity of Titania Containing Gold Nanoparticles for the Generation of Hydrogen or Oxygen from Water. *J. Am. Chem. Soc.* **2011**, *133* (3), 595–602.

(19) Asahi, R. Visible-Light Photocatalysis in Nitrogen-Doped Titanium Oxide. *Science (80-).* **2001**, *293*, 26.

(20) Ansari, S. A.; Khan, M. M.; Ansari, M. O.; Cho, M. H. Nitrogen-Doped Titanium Dioxide (N-Doped TiO_2) for Visible Light Photocatalysis. *New J. Chem.* **2016**, *40* (4), 3000–3009.

(21) Empedocles, S. A.; Bawendi, M. G. Quantum-Confined Stark Effect in Single CdSe Nanocrystallite Quantum Dots. *Science (80-.).* **1997**, *278* (5346), 2114–2117.

(22) Ouisse, T.; Nassiopoulou, A. G. Dependence of the Radiative Recombination Lifetime upon Electric Field in Silicon Quantum Dots Embedded into SiO2. *Europhys. Lett.* **2000**, *51* (2), 168.

(23) Bastard, G.; Mendez, E. E.; Chang, L. L.; Esaki, L. Variational Calculations on a Quantum Well in an Electric Field. *Phys. Rev. B* **1983**, *28* (6), 3241.

(24) Assavachin, S.; Osterloh, F. E. Ferroelectric Polarization in $BaTiO_3$ Nanocrystals Controls Photoelectrochemical Water Oxidation and Photocatalytic Hydrogen Evolution. *J. Am. Chem. Soc.* **2023**, *145* (34), 18825–18833.

(25) Tiewcharoen, S.; Warakulwit, C.; Lapeyre, V.; Garrigue, P.; Fourier, L.; Elissalde, C.; Buffière, S.; Legros, P.; Gayot, M.; Limtrakul, J. Anisotropic Metal Deposition on TiO_2 Particles by Electric- Field- Induced Charge Separation. *Angew. Chemie* **2017**, *129* (38), 11589–11593.

(26) Jiang, Z.; Wang, H.; Huang, H.; Cao, C. Photocatalysis Enhancement by Electric Field:

TiO_2 Thin Film for Degradation of Dye X-3B. *Chemosphere* **2004**, *56* (5), 503–508.

(27) Zhao, Y.; Huang, Z.; Chang, W.; Wei, C.; Feng, X.; Ma, L.; Qi, X.; Li, Z. Microwave-Assisted Solvothermal Synthesis of Hierarchical TiO_2 Microspheres for Efficient Electro-Field-Assisted-Photocatalytic Removal of Tributyltin in Tannery Wastewater. *Chemosphere* **2017**, *179*, 75–83.

(28) Ma, Y.; Bian, X.; Yang, W. Mechanism of the Influence of an Electric Field near the Wire on Photocatalytic Processes Based on First Principles. *AIP Adv.* **2019**, *9* (6), 065005.

(29) Sueda, S.; Yoshida, K.; Tanaka, N. Quantification of Metallic Nanoparticle Morphology on TiO2 Using HAADF-STEM Tomography. *Ultramicroscopy* **2010**, *110* (9), 1120–1127.

(30) Shi, H.; Zhang, S.; Zhu, X.; Liu, Y.; Wang, T.; Jiang, T.; Zhang, G.; Duan, H. Uniform Gold-Nanoparticle-Decorated {001}-Faceted Anatase TiO_2 Nanosheets for Enhanced Solar-Light Photocatalytic Reactions. *ACS Appl. Mater. Interfaces* **2017**, *9* (42), 36907–36916.

(31) Pugazhenthiran, N.; Murugesan, S.; Sathishkumar, P.; Anandan, S. Photocatalytic Degradation of Ceftiofur Sodium in the Presence of Gold Nanoparticles Loaded TiO_2 under UV-Visible Light. *Chem. Eng. J.* **2014**, *241*, 401–409.

(32) Tobaldi, D. M.; Pullar, R. C.; Seabra, M. P.; Labrincha, J. A. Fully Quantitative X-Ray Characterisation of Evonik Aeroxide TiO_2 P25. *Mater. Lett.* **2014**, *122*, 345–347.

(33) Han, C.; Qi, M.-Y.; Tang, Z.-R.; Gong, J.; Xu, Y.-J. Gold Nanorods-Based Hybrids with Tailored Structures for Photoredox Catalysis: Fundamental Science, Materials Design and Applications. *Nano Today* **2019**, *27*, 48–72.

(34) Akita, T.; Tanaka, K.; Kohyama, M.; Haruta, M. HAADF-STEM Observation of Au Nanoparticles on TiO_2. *Surf. Interface Anal.* **2008**, *40* (13), 1760–1763.

(35) Stevanovic, A.; Ma, S.; Yates, J. T. Effect of Gold Nanoparticles on Photoexcited Charge

Carriers in Powdered TiO2-Long Range Quenching of Photoluminescence. *J. Phys. Chem. C* **2014**, *118* (36), 21275–21280.

(36) Das, A.; Dagar, P.; Kumar, S.; Ganguli, A. K. Effect of Au Nanoparticle Loading on the Photo-Electrochemical Response of Au–P25–TiO2 Catalysts. *J. Solid State Chem.* **2020**, *281* (November 2019), 121051.

(37) Han, C.; Li, S.-H.; Tang, Z.-R.; Xu, Y.-J. Tunable Plasmonic Core–Shell Heterostructure Design for Broadband Light Driven Catalysis. *Chem. Sci.* **2018**, *9* (48), 8914–8922.

(38) Hu, D.; Dong, C.; Belhout, S.; Shetty, S.; Ng, H.; Brasseur, P.; Bezerra, L. S.; Ben Tayeb, K.; Simon, P.; Addad, A.; Virginie, M.; Wojcieszak, R.; Ordomsky, V. V.; Camargo, P. H. C.; Khodakov, A. Y. Roles of Titania and Plasmonic Gold Nanoparticles of Different Sizes in Photocatalytic Methane Coupling at Room Temperature. *Mater. Today Energy* **2023**, *36*. 101358.

(39) Dozzi, M. V.; Candeo, A.; Marra, G.; D'Andrea, C.; Valentini, G.; Selli, E. Effects of Photodeposited Gold vs Platinum Nanoparticles on N,F-Doped TiO2 Photoactivity: A Time-Resolved Photoluminescence Investigation. *J. Phys. Chem. C* **2018**, *122* (26), 14326–14335.

(40) Kruse, N.; Chenakin, S. XPS Characterization of Au/TiO2 Catalysts: Binding Energy Assessment and Irradiation Effects. *Appl. Catal. A Gen.* **2011**, *391* (1–2), 367–376.

(41) Wang, M.; Shen, S.; Li, L.; Tang, Z.; Yang, J. Effects of Sacrificial Reagents on Photocatalytic Hydrogen Evolution over Different Photocatalysts. *J. Mater. Sci.* **2017**, *52* (9), 5155–5164.

(42) Zhan, Z.; An, J.; Zhang, H.; Hansen, R. V.; Zheng, L. Three-Dimensional Plasmonic Photoanodes Based on Au-Embedded TiO_2 Structures for Enhanced Visible-Light Water Splitting. *ACS Appl. Mater. Interfaces* **2014**, *6* (2), 1139–1144.

(43) Liu, M.; Jin, X.; Li, S.; Billeau, J.-B.; Peng, T.; Li, H.; Zhao, L.; Zhang, Z.; Claverie, J. P.; Razzari, L. Enhancement of Scattering and Near Field of TiO_2–Au Nanohybrids Using a Silver Resonator for Efficient Plasmonic Photocatalysis. *ACS Appl. Mater. Interfaces* **2021**, *13* (29), 34714–34723.

(44) Luna, M.; Barawi, M.; Gómez-Moñivas, S.; Colchero, J.; Rodríguez-Peña, M.; Yang, S.; Zhao, X.; Lu, Y.-H.; Chintala, R.; Reñones, P. Photoinduced Charge Transfer and Trapping on Single Gold Metal Nanoparticles on TiO2. *ACS Appl. Mater. Interfaces* **2021**, *13* (42), 50531–50538.

(45) Carter, E.; Carley, A. F.; Murphy, D. M. Evidence for O2-Radical Stabilization at Surface Oxygen Vacancies on Polycrystalline TiO2. *J. Phys. Chem. C* **2007**, *111* (28), 10630–10638.

(46) Nie, J.; Schneider, J.; Sieland, F.; Xia, S.; Bahnemann, D. W. The Role of Au Loading for Visible-Light Photocatalytic Activity of Au-TiO_2 (Anatase). *J. Photochem. Photobiol. A Chem.* **2018**, *366*, 111–117.

(47) Kumar, C. P.; Gopal, N. O.; Wang, T. C.; Wong, M.-S.; Ke, S. C. EPR Investigation of TiO_2 Nanoparticles with Temperature-Dependent Properties. *J. Phys. Chem. B* **2006**, *110* (11), 5223–5229.

(48) Zhang, X.; Li, Z.; Zeng, B.; Li, C.; Han, H. EPR Study of Charge Separation Associated States and Reversibility of Surface Bound Superoxide Radicals in $SrTiO_3$ Photocatalyst. *J. Energy Chem.* **2022**, *70*, 388–393.

(49) Yu, W.; Chen, F.; Wang, Y.; Zhao, L. Rapid Evaluation of Oxygen Vacancies-Enhanced Photogeneration of the Superoxide Radical in Nano-TiO_2 Suspensions. *RSC Adv.* **2020**, *10* (49), 29082–29089.

(50) Barrow, S. J.; Rossouw, D.; Funston, A. M.; Botton, G. A.; Mulvaney, P. Mapping Bright and Dark Modes in Gold Nanoparticle Chains Using Electron Energy Loss Spectroscopy. *Nano Lett.* **2014**, *14* (7), 3799–3808.

(51) Eriksen, S.; Egdell, R. G. Electronic Excitations at Oxygen Deficient TiO_2(110) Surfaces: A Study by EELS. *Surf. Sci.* **1987**, *180* (1), 263–278.

(52) Knorr, F. J.; Mercado, C. C.; McHale, J. L. Trap-State Distributions and Carrier Transport in Pure and Mixed-Phase TiO_2: Influence of Contacting Solvent and Interphasial Electron Transfer. *J. Phys. Chem. C* **2008**, *112* (33), 12786–12794.

(53) Shi, J.; Chen, J.; Feng, Z.; Chen, T.; Lian, Y.; Wang, X.; Li, C. Photoluminescence Characteristics of TiO_2 and Their Relationship to the Photoassisted Reaction of Water/Methanol Mixture. *J. Phys. Chem. C* **2007**, *111* (2), 693–699.

(54) Ma, S.; Reish, M. E.; Zhang, Z.; Harrison, I.; Yates, J. T. Anatase-Selective Photoluminescence Spectroscopy of P25 TiO2 Nanoparticles: Different Effects of Oxygen Adsorption on the Band Bending of Anatase. *J. Phys. Chem. C* **2017**, *121* (2), 1263–1271.

(55) Iwata, K.; Takaya, T.; Hamaguchi, H.; Yamakata, A.; Ishibashi, T.; Onishi, H.; Kuroda, H. Carrier Dynamics in TiO_2 and Pt/TiO_2 Powders Observed by Femtosecond Time-Resolved near-Infrared Spectroscopy at a Spectral Region of 0.9− 1.5 Mm with the Direct Absorption Method. *J. Phys. Chem. B* **2004**, *108* (52), 20233–20239.

(56) Tamaki, Y.; Hara, K.; Katoh, R.; Tachiya, M.; Furube, A. Femtosecond Visible-to-IR Spectroscopy of TiO2 Nanocrystalline Films: Elucidation of the Electron Mobility before Deep Trapping. *J. Phys. Chem. C* **2009**, *113* (27), 11741–11746.

(57) Voisin, C.; Del Fatti, N.; Christofilos, D.; Vallée, F. Ultrafast Electron Dynamics and Optical Nonlinearities in Metal Nanoparticles. *The Journal of Physical Chemistry B*. ACS

Publications 2001, pp 2264–2280.

(58) Bryckaert, M.; Kharchenko, A.; Lebedev, O.; Dong, B.; De Waele, I.; Buntinx, G.; Poizat, O.; Mintova, S.; De Waele, V. Hot-Electron Photodynamics of Silver-Containing Nanosized Zeolite Films Revealed by Transient Absorption Spectroscopy. *J. Phys. Chem. C* **2017**, *121* (48), 26958–26966.

(59) Hodak, J. H.; Henglein, A.; Hartland, G. V. Electron-Phonon Coupling Dynamics in Very Small (between 2 and 8 Nm Diameter) Au Nanoparticles. *J. Chem. Phys.* **2000**, *112* (13), 5942–5947.

(60) Pallotti, D. K.; Passoni, L.; Maddalena, P.; Di Fonzo, F.; Lettieri, S. Photoluminescence Mechanisms in Anatase and Rutile TiO_2. *J. Phys. Chem. C* **2017**, *121* (16), 9011–9021.

(61) Yang, Y. H.; Chen, X. Y.; Feng, Y.; Yang, G. W. Physical Mechanism of Blue-Shift of UV Luminescence of a Single Pencil-like ZnO Nanowire. *Nano Lett.* **2007**, *7* (12), 3879–3883.

(62) Bharti, B.; Kumar, S.; Lee, H. N.; Kumar, R. Formation of Oxygen Vacancies and Ti^{3+} State in TiO2 Thin Film and Enhanced Optical Properties by Air Plasma Treatment. *Sci. Rep.* **2016**, *6* (May), 1–12.

(63) Zhang, Y.; Pluchery, O.; Caillard, L.; Lamic-Humblot, A.-F.; Casale, S.; Chabal, Y. J.; Salmeron, M. Sensing the Charge State of Single Gold Nanoparticles via Work Function Measurements. *Nano Lett.* **2015**, *15* (1), 51–55.

(64) Scanlon, D. O.; Dunnill, C. W.; Buckeridge, J.; Shevlin, S. A.; Logsdail, A. J.; Woodley, S. M.; Catlow, C. R. A.; Powell, M. J.; Palgrave, R. G.; Parkin, I. P.; Watson, G. W.; Keal, T. W.; Sherwood, P.; Walsh, A.; Sokol, A. A. Band Alignment of Rutile and Anatase TiO_2. *Nat. Mater.* **2013**, *12* (9), 798–801.

(65) Aluicio-Sarduy, E.; Callegari, S.; del Valle, D. G. F.; Desii, A.; Kriegel, I.; Scotognella,

F. Electric Field Induced Structural Colour Tuning of a Silver/Titanium Dioxide Nanoparticle One-Dimensional Photonic Crystal. *Beilstein J. Nanotechnol.* **2016**, *7* (1), 1404–1410.

(66) Ung, T.; Giersig, M.; Dunstan, D.; Mulvaney, P. Spectroelectrochemistry of Colloidal Silver. *Langmuir* **1997**, *13* (6), 1773–1782.

(67) Novo, C.; Funston, A. M.; Gooding, A. K.; Mulvaney, P. Electrochemical Charging of Single Gold Nanorods. *J. Am. Chem. Soc.* **2009**, *131* (41), 14664–14666.

(68) Luo, C.; Ren, X.; Dai, Z.; Zhang, Y.; Qi, X.; Pan, C. Present Perspectives of Advanced Characterization Techniques in TiO_2-Based Photocatalysts. *ACS Appl. Mater. Interfaces* **2017**, *9* (28), 23265–23286.

(69) Bohren, C. F.; Huffman, D. R. *Absorption and Scattering of Light by Small Particles*; John Wiley & Sons, 2008.

(70) Berciaud, S.; Cognet, L.; Tamarat, P.; Lounis, B. Observation of Intrinsic Size Effects in the Optical Response of Individual Gold Nanoparticles. *Nano Lett.* **2005**, *5* (3), 515–518.

(71) Johnson, P. B.; Christy, R.-Wjp. Optical Constants of the Noble Metals. *Phys. Rev. B* **1972**, *6* (12), 4370.